An International Journal
computers & mathematics with applications

PERGAMON Computers and Mathematics with Applications 43 (2002) 329–350

www.elsevier.com/locate/camwa

Stability Analysis of Particle Methods with Corrected Derivatives

T. BELYTSCHKO AND SHAOPING XIAO
Department of Mechanical Engineering, Northwestern University
2145 Sheridan Road
Evanston, IL 60208, U.S.A.

Abstract—The stability of discretizations by particle methods with corrected derivatives is analyzed. It is shown that the standard particle method (which is equivalent to the element-free Galerkin method with an Eulerian kernel and nodal quadrature) has two sources of instability:

(1) rank deficiency of the discrete equations, and
(2) distortion of the material instability.

The latter leads to the so-called tensile instability. It is shown that a Lagrangian kernel with the addition of stress points eliminates both instabilities. Examples that verify the stability of the new formulation are given. © 2002 Elsevier Science Ltd. All rights reserved.

Keywords—Particle methods, Stability, Kernel.

1. INTRODUCTION

Meshfree methods have recently evolved in two distinct directions:

(1) methods based on field approximations such as moving least square approximations and radial-basis functions, such as the element-free Galerkin (EFG) method [1] and partition-of-unity methods, such as *hp*-clouds [2,3], and
(2) methods based on kernel approximations, which were originated by Lucy [4] and Monaghan [5].

In [6], it is shown that, in some cases, the two methods are closely related. The kernel approximations used in particle methods are somewhat inaccurate because they cannot exactly reproduce linear functions. It has been shown in [6] that if the kernel approximations are corrected so that they reproduce linear functions exactly, then the corrected kernel function is identical to the moving least square approximation with a linear basis in EFG. Liu *et al.* [7] have shown the convergence of these methods in linear elasticity.

A second method for improving the accuracy of particle methods is the correction of the derivatives. This concept was originated for kernel methods by Johnson and Beissel [8], and a better version was reported by Randles and Libersky [9]. Krongauz and Belytschko [10] developed a corrected derivatives method with the Shepard function approximation and studied it in linear problems. The methods of Randles and Libersky [9] and Krongauz and Belytschko [10] have many similarities. The major difference is that the Randles-Libersky form does not exactly

The support of Army Research Office and Office of Naval Research are gratefully acknowledged.

PII: S0898-1221(01)00290-5

satisfy the patch test, as noted in [11]; there are also differences in the treatment of essential boundary conditions. Black and Belytschko [12] have proven that the Krongauz-Belytschko method [10] converges for the Poisson equation. The advantage of derivative correction over function correction is its improved speed.

In this paper, we examine the stability of particle methods based on the Shepard function with corrected derivatives. Since stability analyses are made on infinite domains, differences in boundary treatments are irrelevant and the results also apply to kernel methods with corrected derivatives [10]. In the analysis, we consider both nodal integration, which corresponds to a standard particle method, and stress point stabilization [13,14]. In the stability analysis, we consider one-dimensional and two-dimensional problems. For these cases, we consider both Eulerian and Lagrangian kernels. A kernel is considered Eulerian when it is a function of the spatial (Eulerian) coordinates. Eulerian kernels are customarily used in particle methods. A kernel is Lagrangian if it is a function of the material (Lagrangian) coordinates.

We also examine how closely Lagrangian and Eulerian kernels replicate the standard material instabilities. It is shown that the material instability is not replicated accurately by Eulerian kernels. In fact, the tensile instability is a manifestation of error in the reproduction of material instability by Eulerian kernels. In one dimension, the Lagrangian kernel reproduces the onset of material instability exactly.

The outline of this paper is as follows. We summarize the governing equations and their particle discretization in the next section. Section 3 is the stability analysis in one dimension. In this section, different quadrature schemes with Lagrangian and Eulerian kernels are discussed. The stability properties in two dimensions are studied in Section 4. We show the tensile instability by two examples in Section 5.

2. PARTICLE METHOD WITH CORRECTED DERIVATIVES

2.1. Governing Equations

We consider a problem domain Ω with a reference configuration Ω_R and initial configuration Ω_0. Usually, the initial and reference configurations are coincident, but it is often useful to have an arbitrary reference configuration available. The motion is described by

$$\mathbf{x} = \phi(\mathbf{X}, t), \tag{2.1}$$

where $\mathbf{x}$ are the spatial (Eulerian) coordinates and $\mathbf{X}$ are the material (Lagrangian) coordinates. The above map must be one-to-one except on sets of measure zero (i.e., surfaces in 3D), where points can split into two to model cracking.

The momentum equations are

$$\frac{\partial P_{ji}}{\partial X_j} + \rho_0 b_i = \rho_0 \ddot{u}_i, \tag{2.2}$$

where ρ_0 is the initial density, $\mathbf{P}$ is the nominal stress tensor, $\mathbf{b}$ is the body force, $\mathbf{u}$ is the displacement, and superposed dots denote material time derivatives. We have used standard indicial notation, so repeated indices imply sums in the above and henceforth.

When the current configuration corresponds to the reference configuration, i.e., when $\Omega_R = \Omega$, the above form of the momentum equations becomes the spatial form of the momentum equations

$$\frac{\partial \sigma_{ji}}{\partial x_j} + \rho b_i = \rho \ddot{u}_i, \tag{2.3}$$

where ρ is the current density. By conservation of mass,

$$\rho J = \rho_0, \tag{2.4}$$

where J is the Jacobian determinant defined by

$$J = \det(\mathbf{F}), \qquad F_{ij} = \frac{\partial x_i}{\partial X_j}. \tag{2.5}$$

The two above forms of momentum equations are identical and differ in form only because they are expressed in a different description; see [15].

In this paper, we first consider the one-dimensional case. From (2.2) and (2.3), the momentum equation under uniaxial strain in the absence of body forces is

$$\frac{\partial P(X,t)}{\partial X} = \rho_0 \frac{\partial^2 u(X,t)}{\partial t^2}, \qquad \frac{\partial \sigma(x,t)}{\partial x} = \rho \frac{D^2 u(x,t)}{Dt^2}, \tag{2.6}$$

where the above left and right are the Lagrangian and Eulerian forms, respectively, and $P = P_{11}$, $u = u_1$, $\sigma = \sigma_{11}$.

2.2. Meshless and Particle Approximations

We will develop the discrete equations in terms of moving least square approximations. However, the resulting discrete equations are identical to corrected forms of SPH (as in [9]).

An essential building block in meshless approximations is the weight function

$$w_I(\mathbf{X}) = w(\mathbf{X} - \mathbf{X}_I) = \frac{W(\mathbf{X} - \mathbf{X}_I)}{\sum W(\mathbf{X} - \mathbf{X}_I)}, \tag{2.7}$$

which is the moving least square approximation that reproduces the constant function. In SPH, $w(\mathbf{X} - \mathbf{X}_I)$ is called a kernel function or smoothing function. In approximation theory, the MLS approximation to a constant is called a Shepard function [16]. In this paper, we use a quartic spline weight function

$$W(s) = \begin{cases} 1 - 6s^2 + 8s^3 - 3s^4, & \text{for } s \le 1, \\ 0, & \text{for } s > 1, \end{cases} \tag{2.8}$$

and the exponential weight function

$$W(s) = \begin{cases} e^{-(s/0.4)^2}, & \text{for } s \le 1, \\ 0, & \text{for } s > 1, \end{cases} \tag{2.9}$$

where $s = r/h$, $r = \|\mathbf{X} - \mathbf{X}_I\|$, and h is a measure of the size of the support, which is determined by a dilation parameter D_{mx}. We define $h = D_{mx}\Delta X$ for uniformly spaced particles in one dimension. The weight function is of compact support, i.e., $w_I(\mathbf{X}) > 0$ only in the neighborhood of $\mathbf{X}$. The approximation for the displacement is

$$u_i^h(\mathbf{X}, t) = \sum_J w_J(\mathbf{X}) u_{iJ}(t). \tag{2.10}$$

It should be noted that in the above, the kernel $w_J(\mathbf{X})$ is a function of the material coordinates, so we call it a Lagrangian kernel. The above approximation reproduces constant functions exactly, i.e., when $u_{iJ} = 1$, $u_i^h(\mathbf{X}, t) = 1$.

A correction that enables the derivatives of constant or linear fields to be reproduced exactly is developed by Krongauz and Belytschko [10] and Belytschko *et al.* [17]. We will explain the corrected derivatives method concept for multidimension first. The corrected derivatives are denoted by $L_{ji}(\mathbf{X})$ and are approximated by

$$L_{ji}(\mathbf{X}) = \sum_I G_{iI}(\mathbf{X}) u_{jI}, \tag{2.11}$$

where G_{iI} are linear combinations of the derivatives of the Shepard functions. Note that $L_{ji}(\mathbf{X})$ differs from $\frac{\partial u_j^h}{\partial X_i}$ with u_j^h defined by equation (2.10). The approximation functions for the derivatives G_{iI} are defined as linear combinations of the exact derivatives by

$$G_{iI}(\mathbf{X}) = a_{ij}(\mathbf{X}) w_{I,j}(\mathbf{X}), \tag{2.12}$$

where a_{ij} are arbitrary parameters which are determined by the reproducing conditions developed next (note repeated indices are summed).

The reproducing condition for derivative of a linear function can be stated as follows: if the nodal values of the displacement u_{jI} are given by the nodal coordinates X_{jI}, then the derivative should be 1 if $i = j$, 0, otherwise, i.e.,

$$\sum G_{iI} X_{Ij} = \delta_{ij}. \tag{2.13}$$

The above can be written in matrix form as

$$\mathbf{A}\mathbf{a}^{\mathbf{T}} = \mathbf{I}, \tag{2.14}$$

where $\mathbf{I}$ is the identity matrix and for a three-dimensional approximation,

$$\mathbf{A} = \begin{bmatrix} w_{I,X} X_I & w_{I,Y} X_I & w_{I,Z} X_I \\ w_{I,X} Y_I & w_{I,Y} Y_I & w_{I,Z} Y_I \\ w_{I,X} Z_I & w_{I,Y} Z_I & w_{I,Z} Z_I \end{bmatrix}, \tag{2.15}$$

$$\mathbf{a} = \begin{bmatrix} a_{XX} & a_{XY} & a_{XZ} \\ a_{YX} & a_{YY} & a_{YZ} \\ a_{ZX} & a_{ZY} & a_{ZZ} \end{bmatrix}. \tag{2.16}$$

By solving these equations, the corrected gradient function $G_{iI}(\mathbf{X})$, (2.12) can be obtained. The approximation for the derivatives of the displacement is then

$$L_{ji}(\mathbf{X}) = \sum a_{ik}(\mathbf{X}) w_{I,k}(\mathbf{X}) u_{jI}. \tag{2.17}$$

In one dimension, the corrected derivatives are

$$L(\mathbf{X}) = \sum a(\mathbf{X}) w_{I,X}(\mathbf{X}) u_I, \tag{2.18}$$

where

$$G_I(\mathbf{X}) = a(\mathbf{X}) w_{I,X}(\mathbf{X}) \tag{2.19}$$

and

$$a(\mathbf{X}) = \frac{1}{\sum w_{I,X}(\mathbf{X}) X_I}. \tag{2.20}$$

2.3. Discrete Equations

The discrete momentum equation is obtained by the Galerkin weak form. With a Lagrangian kernel, the weak form of the linear momentum conservation equation is

$$\int_{\Omega_0} \delta u_i \rho_0 \ddot{u}_i \, d\Omega = \int_{\Omega_0} \delta u_i \rho_0 b_i \, d\Omega - \int_{\Omega_0} \frac{\partial(\delta u_i)}{\partial X_j} P_{ji} \, d\Omega + \int_{\Gamma_0^t} \delta u_i \bar{t}_i \, d\Gamma, \tag{2.21}$$

where δu_i is the test function, b_i is the body force, and $\bar{t}_i$ is the boundary traction. Substituting the particle approximation (2.10),(2.18) into (2.21) and using a diagonal mass matrix, we have

$$m_I \ddot{u}_{iI} = f_{iI}^{\text{ext}} - f_{iI}^{\text{int}}, \qquad m_{iI} = \rho_0 V_{iI}^0, \tag{2.22}$$

where f_{iI}^{ext}, f_{iI}^{int} are the external and internal nodal forces, respectively, given by

$$f_{iI}^{\text{ext}} = \int_{\Omega_0} \rho_0 w_I b_i \, d\Omega_0 + \int_{\Gamma_0^t} w_I \bar{t}_i \, d\Gamma, \tag{2.23}$$

$$f_{iI}^{\text{int}} = \int_{\Omega_0} \frac{\partial w_I}{\partial X_j}(\mathbf{X}) P_{ji} \, d\Omega_0 = \int_{\Omega} w_{I,x_j}(\mathbf{x}) \sigma_{ji} \, d\Omega, \tag{2.24}$$

where Ω is the current domain; see [15].

2.4. Integration Schemes

2.4.1. Nodal integration

To obtain the discrete momentum equations from the weak form, the integrals of the right-hand sides of (2.23) and (2.24) need to be evaluated by numerical quadrature. In the element-free Galerkin method, background elements or voxels are needed [1]. Beissel and Belytschko [18] have proposed nodal quadrature for the element-free Galerkin method, where any integral is evaluated by summing the function at the nodes, i.e.,

$$\int_{\Omega_0} G(\mathbf{X})\, d\Omega = \sum_I G(\mathbf{X}_I) V_I^0, \tag{2.25}$$

where $V_I^0 = m_I/\rho_0$ is the volume associated with node I. The internal nodal forces (2.24) are then computed by

$$f_{iI}^{\text{int}} = \sum_J V_J^0 \frac{\partial w_I(\mathbf{X}_J)}{\partial X_j} P_{ji}(\mathbf{X}_J). \tag{2.26}$$

This approach was found to be unstable by Beissel and Belytschko [18], which is verified here for the corrected derivative approach also.

Nodal quadrature leads to discrete equations to be collocation equations used in SPH.

2.4.2. Stress point integration

One approach to stabilizing nodal quadrature is to use additional quadrature points called stress points or slave points. In this approach, slave particles are added to the original set of particles (the original particles are called master particles; see Figure 1). The nomenclature "slave" nodes originates in finite element methods, where slave nodes are nodes whose motion is completely determined by the motion of master nodes through kinematic relations. This concept holds where the kinematic variables of slave particles, such as displacement and velocity, are evaluated from the neighboring master particles by integration (2.10). The slave particles are used only for the integration of the Galerkin weak form; the discrete momentum equations are not enforced at the slave nodes, since the displacement of the slave nodes is not arbitrary. The displacement and velocity at the slave particles (stress points), according to (2.10), are

$$u_I^s = \sum_J w_J(X_I^s)\, u_J^m, \qquad v_I^s = \sum_J w_J(X_I^s)\, v_J^m, \tag{2.27}$$

where X_I^s is the material coordinate of a slave particle. The internal nodal forces (2.24) are given by

$$f_{iI}^{\text{int}} = \sum_{J\in\mathcal{N}_m} V_J^{0m} \frac{\partial w_I(\mathbf{X}_J^m)}{\partial X_j} P_{ji}(\mathbf{X}_J^m) + \sum_{J\in\mathcal{N}_s} V_J^{0s} \frac{\partial w_I(\mathbf{X}_J^s)}{\partial X_j} P_{ji}(\mathbf{X}_J^s), \tag{2.28}$$

where $\mathcal{N}_m$, $\mathcal{N}_s$ are the sets of master and slave particles, respectively, which contribute to the master particle at X_I^m. The volumes V_J^{0m} and V_J^{0s} are computed from a Voronoi diagram (see Figure 1) so that

$$\sum_J^{N_m} V_J^{0m} + \sum_J^{N_s} V_J^{0s} = V^0. \tag{2.29}$$

In the above, V^0 is the initial total volume, and N_m and N_s are the number of master particles and stress points in the model, respectively. Note that the volume for the master particle I, V_I^{0m}, differs from the volume associated with the mass V_I^0, as in equation (2.22). The second term on the RHS of (2.28) is the contribution of the slave particle stresses to the master particle forces. The discrete equations of motion (2.22) apply only at the master particles.

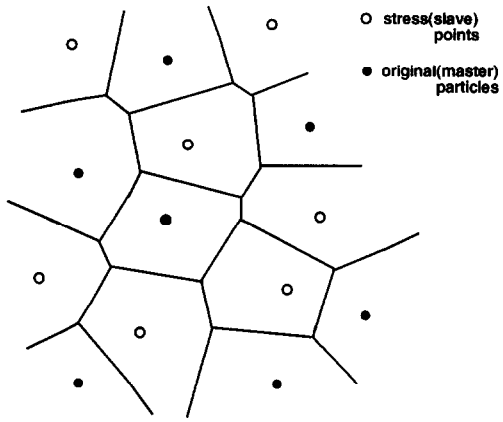

Figure 1. Stress point integration with Voronoi cells for quadrature.

3. STABILITY ANALYSIS IN 1D

In the following, we give a linearized stability analysis of the discrete equations for the particle method (see [19,20]); this is often called a von Neumann stability analysis. We consider an infinite slab under a uniform state of stress. The solution is perturbed by harmonics of various wavelengths. We consider the response stable if it decays or remains constant in amplitude, and unstable if it grows. A response is asymptotically stable if it decays to zero as time goes to infinity.

3.1. Nodal Integration

3.1.1. Lagrangian kernel

We first consider a one-dimensional stability analysis with a Lagrangian kernel with nodal integration. For a plane wave in the X-direction, the only nontrivial components of the relevant tensors are the X components. So the relevant component of the deformation gradient is $F_{11} = F$ (we drop the subscripts in the following), and it is given by

$$F(X) = 1 + \frac{\partial u}{\partial X} = 1 + \sum_J G_J(X) u_J. \tag{3.1}$$

For the Lagrangian kernel with nodal integration, the internal nodal force is given by (2.26), which for the 1D case is given by

$$f_I^{\text{int}} = \sum_J V_J^0 w_{I,X}(X_J) P_J, \qquad V_J^0 = \frac{m_J}{\rho_{0J}}. \tag{3.2}$$

Then the discrete momentum equations are

$$m_I \ddot{u}_I = f_I^{\text{ext}} - \sum_J \frac{m_J}{\rho_{0J}} w_{I,X}(X_J) P_J. \tag{3.3}$$

We consider a material for which the constitutive rate relationship is

$$\dot{P} = \left(C^{SE} F^2 + P F^{-1}\right) \dot{F} = \bar{C} \dot{F}, \qquad \text{where } \bar{C} = C^{SE} F^2 + P F^{-1}. \tag{3.4}$$

The above constant $\bar{C}$ corresponds to the relevant component of the first elasticity tensor, and C^{SE} is the tangent modulus of the relation between the rate of the second Piola-Kirchhoff

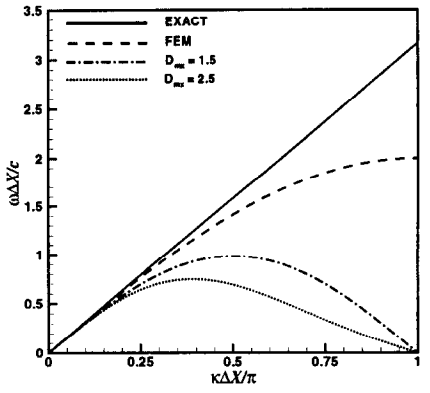

Figure 2. Frequency relations in plane wave by particle method nodal integration with Lagrangian kernel.

stress and the Green strain; see [21] or [15, Section 6]. We use a Fourier representation of the perturbed displacement

$$\tilde{u}_I = g\, e^{i\kappa X_I + i\omega t}, \tag{3.5}$$

where κ is wave number and ω is frequency; both can be complex. The perturbed fields are

$$u(X,t) = u_0(X,t) + \tilde{u}(X,t), \tag{3.6}$$

$$P(X,t) = P_0(X,t) + \tilde{P}(X,t), \tag{3.7}$$

where u_0 and P_0 satisfy the momentum equation. The perturbed momentum equation is

$$m_I \ddot{\tilde{u}}_I = -\sum_J V_J^0 w_{I,X}(X_J)\tilde{P}_J, \tag{3.8}$$

where a superposed tilde denotes a perturbed quantity. From (3.4) and (3.1), it follows that

$$\tilde{P}_I = \bar{C}\tilde{F}_I, \qquad \tilde{F}_I = \sum_J G_J(X_I)\tilde{u}_J, \qquad \bar{C}_0 = C^{SE}F_0^2 + P_0 F_0^{-1}. \tag{3.9}$$

Substituting the above into equation (3.8) yields the dispersion equation

$$\omega^2 = \frac{1}{m_I}\sum_J V_J^0 w_{I,X}(X_J)\bar{C}\left\{\sum_K G_K(X_J)\cos[\kappa(X_K - X_I)]\right\}. \tag{3.10}$$

In an infinite domain, for identical, uniformly spaced nodes and a symmetric weight function, we have $m_I = m_0$, $V_I^0 = V^0 = m_0/\rho_0$, and

$$\phi_I(X_J) = \phi_J(X_I), \qquad G_I(X_J) = -G_J(X_I), \qquad w_{I,X}(X_J) = -w_{J,X}(X_I). \tag{3.11}$$

Consider a generic particle I with $X_I = 0$; then equation (3.10) can be written as

$$\omega^2 = \frac{a\bar{C}}{\rho_0}\left[\sum_j w_{,X}(j\Delta X)\sin(\kappa j\Delta X)\right]^2, \tag{3.12}$$

where a is the correction factor, which is constant in an infinite domain; j are the nodes in the support of the weight function of node I if we let $I = 0$. When $D_{mx} = 1.5$, the range of j is -1 to 1.

The relationships between frequency and wave number are shown in Figure 2. As can be seen from (3.5), the response is unstable if the imaginary part of ω is negative, i.e., if $\mathrm{Im}(\omega) < 0$. We have also shown the results for a mesh of two-node finite elements. Two interesting features appear in these results.

(1) An instability occurs at $\kappa = \pi/\Delta X$, regardless of the state of stress or the material tangent modulus. This is the cut-off wave number for a uniform nodal spacing ΔX. This implies the existence of a spurious singular mode in the discrete equations. This instability is similar to that found in finite elements due to rank deficiency. A system is considered to be rank deficient when the rank of the linear equations for the system is lower than the proper rank, which equals the number of degrees of freedom minus the number of rigid body modes; see [15, Section 8]. This instability occurs regardless of the size of the support.

(2) The response is unstable when $\bar{C} = 0$; this is desirable, since the continuum equations are also unstable when the first elasticity tensor vanishes. The instability associated with the vanishing of the tangent modulus $\bar{C}$ is called a material instability; see [21]. Note that the onset of the material instability in both the continuum and this discretization depends on the initial stress P_0.

It can also be seen that the dispersion error of the particle methods exceeds that of finite elements.

3.1.2. Eulerian kernel

For an Eulerian kernel with nodal integration, the internal nodal force is

$$f_I^{\text{int}} = \sum_J V_J w_{I,x}(x_J)\sigma_J, \qquad V_J = \frac{m_J}{\rho_J} = \frac{m_J F_J}{\rho_{0J}} = V_J^0 F_J, \tag{3.13}$$

and the discrete equations are

$$\begin{aligned} m_I \ddot{u}_I &= f_I^{\text{ext}} - \sum_J \frac{m_J}{\rho_{0J}} w_{I,x}(x_J)\sigma_J F_J, \\ F_I &= \frac{1}{1 - \frac{\partial u}{\partial x}\big|_I}, \qquad \frac{\partial u}{\partial x}\bigg|_I = \sum_J g_J(x_I) u_J. \end{aligned} \tag{3.14}$$

The perturbed equation (3.14) is

$$m_I \ddot{\tilde{u}}_I = -\sum_J \frac{m_J}{\rho_{0J}} \left[w_{I,x}(x_J) \left(\tilde{\sigma}_J F_J + \sigma_J \tilde{F}_J \right) + \sigma_J F_J \tilde{w}_{I,x}(x_J) \right], \tag{3.15}$$

where

$$\begin{aligned} \tilde{w}_{I,x}(x_J) &= w_{I,xx}(x_J)\left(\tilde{u}_J - \tilde{u}_I\right), \\ \tilde{\sigma}_I = \tilde{P}_I &= \bar{C}' F_I^{-1} \tilde{F}_I, \qquad \tilde{F}_I = \frac{\partial \tilde{u}}{\partial X}\bigg|_I = F_I \sum_J g_J(x_I)\tilde{u}_J, \end{aligned} \tag{3.16}$$

and $\bar{C}'$ is the counterpart of equation (3.4) in the current configuration (see [15]).

$$\bar{C}' = \left(C^{\sigma\mathcal{T}} + \sigma\right), \qquad C^{\sigma\mathcal{T}} = C^{SE} F^3, \tag{3.17}$$

where $C^{\sigma\mathcal{T}}$ relates the Truesdell rate of the Cauchy stress to the rate-of-deformation, so in one dimension, $\dot{\sigma} = (C^{\sigma\mathcal{T}} + \sigma)D$.

Substituting (3.16) into (3.15) gives the dispersion equation, which for a symmetric weight function and identical particles in an infinite domain is

$$\begin{aligned} \omega^2 = \frac{a\bar{C}'}{\rho} &\left[\sum_j w_{,x}(j\Delta x) \sin(\kappa j \Delta x) \right]^2 \\ - \frac{\sigma}{\rho} &\left\{ \sum_j w_{,xx}(j\Delta x)\left[1 - \cos(\kappa j \Delta x)\right] - a \left[\sum_j w_{,x}(j\Delta x)\sin(\kappa j \Delta x) \right]^2 \right\}. \end{aligned} \tag{3.18}$$

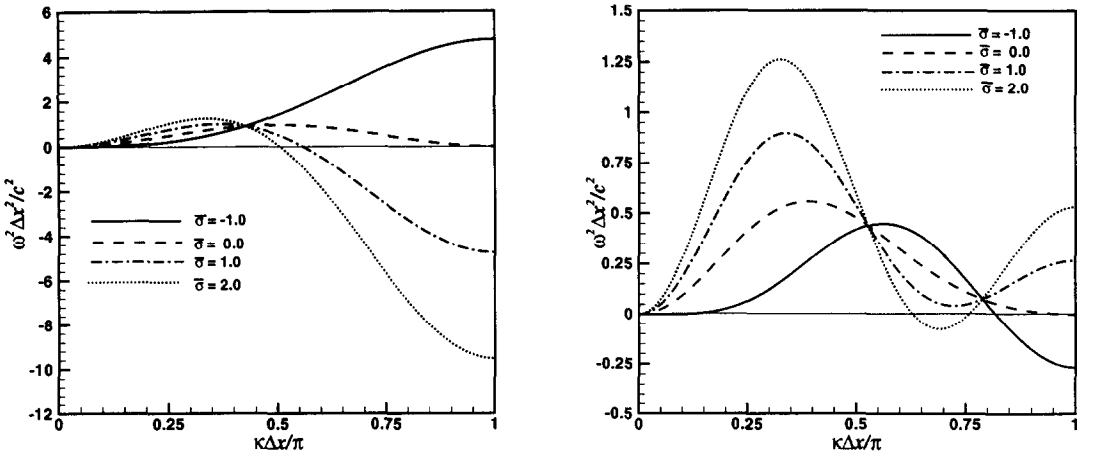

(a) $D_{\text{mx}} = 1.5$. (b) $D_{\text{mx}} = 2.5$.

Figure 3. Frequency-wave number relations in plane wave by particle method with nodal integration and Eulerian kernel for $C^{\sigma T} > 0$; $c^2 = C^{\sigma T}/\rho$.

There are several very interesting features to this result. First of all, ω^2 does not vanish when $\bar{C}' = 0$, so the discrete equations do not always exhibit an instability when $\bar{C}' = 0$. This contradicts the behavior of the continuum equations, which always exhibit a material instability when $\bar{C}' \leq 0$. There are two instabilities:

(1) the spurious singular mode $u_I = (-1)^I$ at the cutoff wave number $\kappa = \pi/\Delta x$;
(2) an instability occurs when $\sigma > 0$ and $\bar{C}' \neq 0$; this is the tensile instability identified by Swegle *et al.* [22].

Figure 3 shows the frequency-wave number as a function of the normalized stress ($\bar{\sigma} = \sigma/C^{\sigma T}$) for different support sizes ($h = D_{\text{mx}}\Delta x$), for a quartic spline weight function with a positive elasticity tensor ($C^{\sigma T} > 0$). Figure 4 shows the same relationship, but with a negative elasticity tensor ($C^{\sigma T} < 0$).

In Figure 3 for $D_{\text{mx}} = 1.5$, the frequency becomes imaginary for $\bar{\sigma} = 1$, i.e., a tensile stress if the wave number κ is greater than about $0.6\pi/\Delta x$. This corresponds to the tensile instability. As $\bar{\sigma}$ increases, the wave number for the onset of instability decreases. For $D_{\text{mx}} = 2.5$, as seen in Figure 3, the tensile stress required for the onset of instability is greater, but the tensile instability remains. When $\bar{\sigma} = -1$, $\bar{C}' = 0$, it is stable for $D_{\text{mx}} = 1.5$. When $D_{\text{mx}} = 2.5$, it is also stable for most frequencies.

When $C^{\sigma T} < 0$, Figure 4 shows that the behavior is even more complex. For $D_{\text{mx}} = 1.5$, the response is unstable at all frequencies, which is exactly the behavior found in a material instability. However, for $D_{\text{mx}} = 2.5$, there are ranges of frequency in which the discrete response is stable even if $\bar{C}' < 0$.

In summary, it can be seen that the particle equations with an Eulerian kernel distort the onset of material instability and exhibit a tensile instability. On the other hand, the Lagrangian kernel *does not exhibit the tensile instability* regardless of the magnitude of the tensile stress and reproduces the onset of material instability exactly.

From (3.12) and (3.18), we can obtain the relations between normalized stress and wave number for the threshold frequency; i.e., $w^2 = 0$. Figures 5 and 6 show the stable fields and unstable domains. For a Lagrangian kernel, it becomes unstable when $\bar{\sigma} = -1$, i.e., $\bar{C} = 0$ no matter what the wave number is. This is a material instability that also occurs in the PDE which governs the continuum. However, for Eulerian kernel, the onset of this instability does not replicate the material instability. In other words, due to the character of the discretization, the Eulerian kernel distorts the material instability.

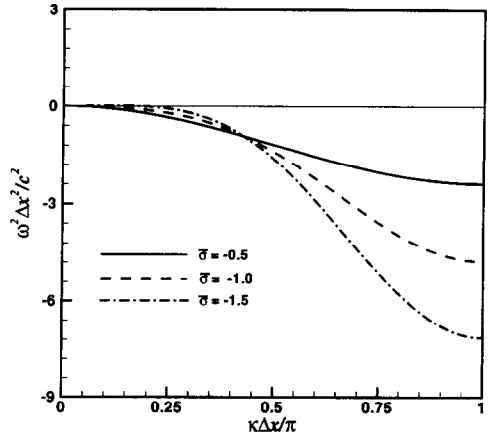

(a) $D_{\mathrm{mx}} = 1.5$.

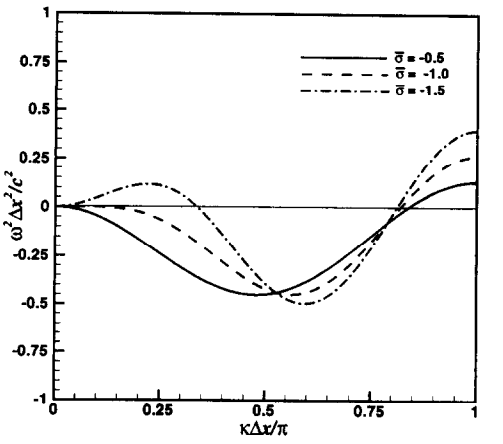

(b) $D_{\mathrm{mx}} = 2.5$.

Figure 4. Frequency-wave number relations in plane wave by particle method with nodal integration and Eulerian kernel for $C^{\sigma T} < 0$; $c^2 = -C^{\sigma T}/\rho$.

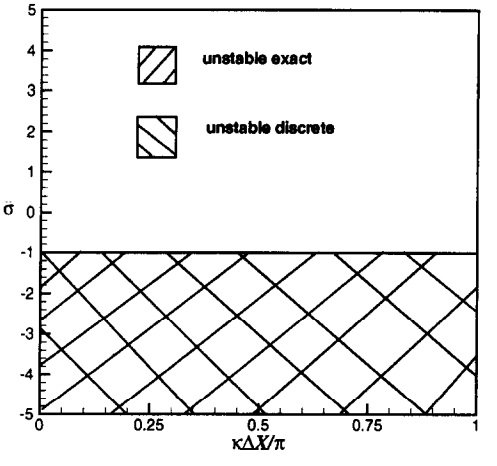

(a) $C^{\sigma T} > 0$.

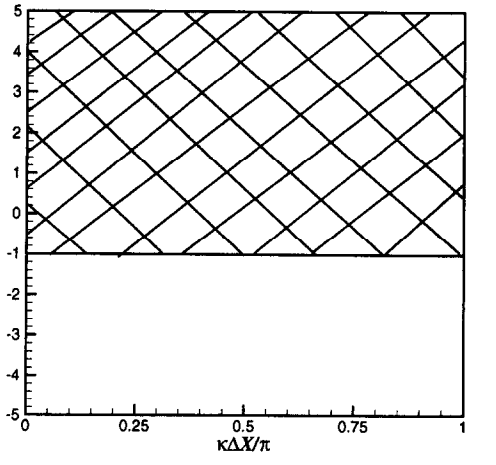

(b) $C^{\sigma T} < 0$.

Figure 5. Stable and unstable domains for Lagrangian kernel as compared to the exact domain.

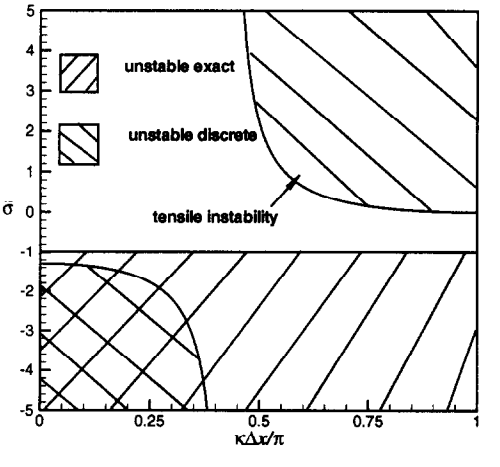

(a) $C^{\sigma T} > 0$.

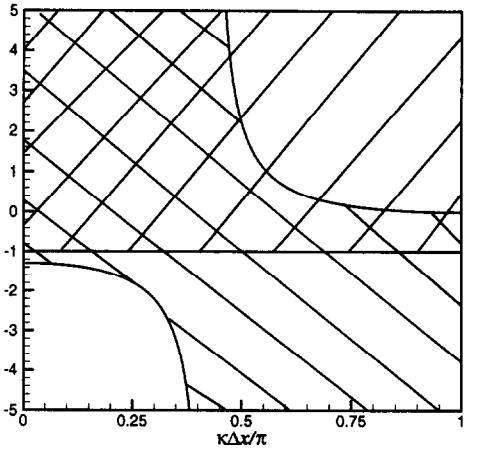

(b) $C^{\sigma T} < 0$.

Figure 6. Stable and unstable domains for Eulerian kernel as compared to the exact domain.

3.2. Stress Point Integration

In the following, we show that the Lagrangian kernel with stress points eliminates the instability due to rank deficiency and correctly replicates the material instability.

We examine the stability of Lagrangian kernels with stress points for a uniform particle distribution in one dimension. We place stress points at the center of each interval. The internal nodal force is obtained by specializing (2.27),

$$f_I^{\text{int}} = \sum_{J \in \mathcal{N}_m} V_J^{0m} w_{I,X}\left(X_J^m\right) P_J^m + \sum_{J \in \mathcal{N}_s} V_J^{0s} w_{I,X}\left(X_J^s\right) P_J^s, \tag{3.19}$$

where $\mathcal{N}_m$, $\mathcal{N}_s$ are the sets of master particles and stress points contributing to the integral. Thus, the perturbed momentum equation is

$$m_I \ddot{\tilde{u}}_I = -\sum_{J \in \mathcal{N}_M} V_J^{0m} w_{I,X}\left(X_J^m\right) \tilde{P}_J^m - \sum_{J \in \mathcal{N}_S} V_J^{0s} w_{I,X}\left(X_J^s\right) \tilde{P}_J^s. \tag{3.20}$$

Note that the volume V^{0m} differs from V^0 for the master particles. The stresses are calculated from the displacements of supporting master particles by

$$\tilde{P}_J^m = \bar{C}\tilde{F}_J^m = \bar{C}\sum_K G_K\left(X_J^m\right)\tilde{u}_K, \qquad \tilde{P}_J^s = \bar{C}\tilde{F}_J^s = \bar{C}\sum_K G_K\left(X_J^s\right)\tilde{u}_K. \tag{3.21}$$

By algebra similar to that in the preview section, we obtain the following dispersion equation:

$$\begin{aligned}\omega^2 = \frac{1}{m_I^0}\Bigg\{ &\sum_{J \in \mathcal{N}_m} V_J^{0m} w_{I,X}\left(X_J^m\right)\bar{C}\left[\sum_K G_K\left(X_J^m\right)\cos\left[\kappa\left(X_K^m - X_I^m\right)\right]\right] \\ &+ \sum_{J \in \mathcal{N}_s} V_J^{0s} w_{I,X}\left(X_J^s\right)\bar{C}\left[\sum_K G_K\left(X_J^s\right)\cos\left[\kappa\left(X_K^m - X_I^m\right)\right]\right]\Bigg\}.\end{aligned} \tag{3.22}$$

For an infinite bar of uniformly spaced particles, the above can be written as

$$\omega^2 = \frac{\bar{C}}{2\rho_0}\left[a_m\left(\sum_{j_m} w_{j,X} s_j\right)^2 + a_s\left(\sum_{j_s} \bar{w}_{j,X}\bar{s}_j\right)^2\right]. \tag{3.23}$$

Here, we have set $I = 0$ and

$$\begin{aligned} s_j &= \sin\left(\kappa j_m \Delta X\right), & \bar{s}_j &= \sin\left(\kappa\left(j_s + \frac{1}{2}\right)\Delta X\right), \\ w_{j,X} &= w_{,X}(j_m \Delta X), & \bar{w}_{j,X} &= w_{,X}\left(\left(j_S + \frac{1}{2}\right)\Delta X\right), \end{aligned} \tag{3.24}$$

and a_m and a_s are the correction factor for master particles and slave particles. j_m and j_s are the local integers because we set $I = 0$. For $D_{mx} = 1.5$, j_m will be -1 to 1 and j_s will be -2 to 1.

The frequency-wave number relations are shown in Figure 7a for various support sizes ($h = D_{\text{mx}}\Delta X$) and a quartic spline weight function. It can be seen that there are no unstable modes due to rank deficiency at the cutoff wave number. However, the frequency is very small near the

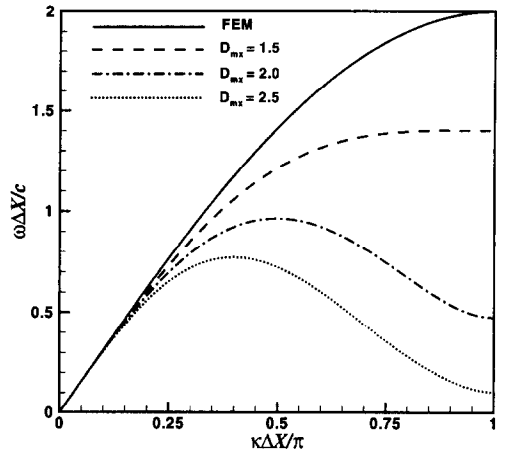

(a) Quartic spline.

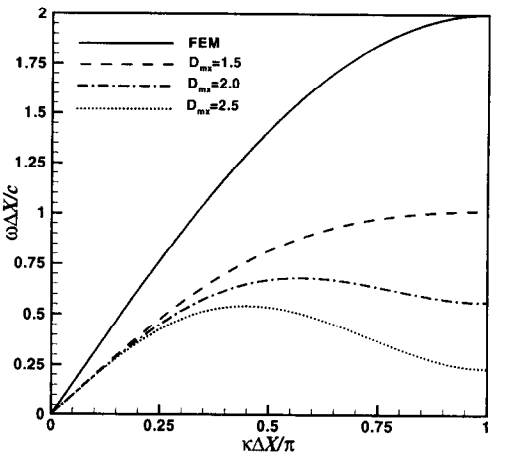

(b) Exponential.

Figure 7. Frequency relations in plane wave by EFG with stress points Lagrangian kernel with lumped mass.

cut-off point for large support size ($D_{\text{mx}} \geq 2.5$). This indicates that we are close to instability for large supports.

At the cut-off wave number ($\kappa = \pi/\Delta X$), equation (3.23) can be written as

$$\omega^2 = \frac{a_s \bar{C}}{2\rho_0} \left(\sum_{j_s} \bar{w}_{j,X} \bar{s}_j \right)^2 = \frac{a_s \bar{C}}{2\rho_0} (\mathbf{WS})^2, \tag{3.25}$$

where $\mathbf{W} = \{\bar{w}_{j,X}\}$, $\mathbf{S} = \{\bar{s}_j\}$. With $D_{mx} = 1.5$ (range of j_s is -2 to 1),

$$\mathbf{W} = \{-b, -a, a, b\}^{\top}, \qquad \mathbf{S} = \{1, -1, 1, -1\}^{\top}, \tag{3.26}$$

where a and b are positive and $a \gg b$, and thus,

$$\omega^2 = \frac{a_s \bar{C}}{2\rho_0} (2(a-b))^2. \tag{3.27}$$

When $D_{mx} = 2.5$ (j_s are -3 to 2), $\mathbf{W} = \{-c, -b, -a, a, b, c\}^{\top}$, $\mathbf{S} = \{-1, 1, -1, 1, -1, 1\}^{\top}$, where a, b, and c are positive and $a > b \gg c$, and thus,

$$\omega^2 = \frac{a_s \bar{C}}{2\rho_0} (2(a-b+c))^2. \tag{3.28}$$

It is obvious that with increasing support size, the frequency decreases at the wave number $\kappa = \pi/\Delta X$. For the exponential weight function, the discretization, as in Figure 7b, is more stable than for quartic spline weight function. We believe this is due to the fact that this weight function is more concentrated about its node than the quartic spline weight function. The peaks of these plots are different because the correction factors a_s are different.

For comparison, the dispersion relation for the two-node linear displacement finite element with lumped mass is also given in this Figure 7. It can be seen that the frequency given by the EFG methods is lower than that of FEM, especially for large wave numbers, the discretization is more dispersive. Moreover, it can be seen that the high-frequency accuracy of particle methods is less than that of FEM.

4. STABILITY ANALYSIS IN 2D

To investigate whether our findings apply to higher-dimensional problems, we consider a two-dimensional plane wave motion in an infinite domain. Two arrangements of particles are considered: rectangular and hexagonal. For nodal integration, nodes are connected to form a virtual quadrilateral or triangles. For stress points, slave nodes are placed in the centers of virtual quadrilaterals or triangles (see Figure 8, where the filled circles indicate the master particles and the empty circles denote the stress points).

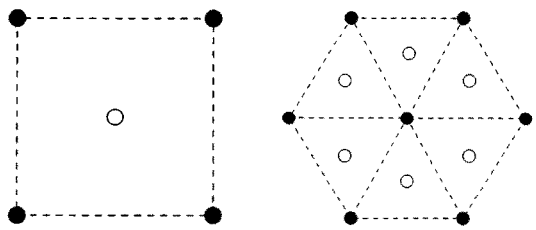

(a) Center of quadrilateral. (b) Hexagonal shape.

Figure 8. Positions of stress points in two-dimensional meshes.

4.1. Nodal Integration

4.1.1. Lagrangian kernel

In 2D, for nodal integration with a Lagrangian kernel, the discrete perturbed momentum equation is

$$m_I \ddot{\tilde{u}}_i(\mathbf{X}_I) = -\tilde{f}_{iI}^{\text{int}} = -\sum_{J\in\mathcal{N}} V_J^0 w_{I,j}(\mathbf{X}_J)\tilde{P}_{ji}(\mathbf{X}_J). \tag{4.1}$$

The perturbed stress is given by

$$\tilde{P}_{ij} = \bar{C}_{ijrl}\tilde{F}_{rl}, \tag{4.2}$$

where

$$\bar{C}_{ijrl} = C_{ikab}^{SE}F_{rk}F_{js} + S_{il}\delta_{jr}, \qquad \tilde{F}_{rl} = \sum_K G_{lK}(\mathbf{X}_J)\tilde{u}_r(\mathbf{X}_K). \tag{4.3}$$

The perturbation is

$$\tilde{u}_r(\mathbf{X}_K) = A_r e^{i\kappa(X_K\cos\theta + Y_K\sin\theta)+i\omega t}. \tag{4.4}$$

In a plane wave, $A_X = A\cos\theta$ and $A_Y = A\sin\theta$. θ is the direction of the normal direction of the wave front. Then, the above can be written as

$$\tilde{u}_r(\mathbf{X}_K) = A\theta_r e^{i\kappa(X_K\theta_X + Y_K\theta_Y)+i\omega t}, \tag{4.5}$$

where $\theta_X = \cos\theta$ and $\theta_Y = \sin\theta$.

Substituting equations (4.2) and (4.4) into equation (4.1), we obtain the dispersion equation

$$\omega^2 = \frac{1}{m_I(\theta_X+\theta_Y)}\sum_{i\in 2}\sum_{J\in\mathcal{N}} V_J^0 w_{I,j}(\mathbf{X}_J)\bar{C}_{ijrl}\theta_r S_l(\mathbf{X}_J), \tag{4.6}$$

where

$$\begin{aligned} S_l(\mathbf{X}_J) &= \sum_K G_{lK}(\mathbf{X}_J)c_{KI}, \\ c_{KI} &= \cos[\kappa(X_K\theta_X + Y_K\theta_Y) - \kappa(X_I\theta_X + Y_I\theta_Y)]. \end{aligned} \tag{4.7}$$

In 2D plane strain,

$$C_{ijkl}^{SE} = \lambda\delta_{ij}\delta_{kl} + \mu\left(\delta_{ik}\delta_{jl} + \delta_{il}\delta_{jk}\right). \tag{4.8}$$

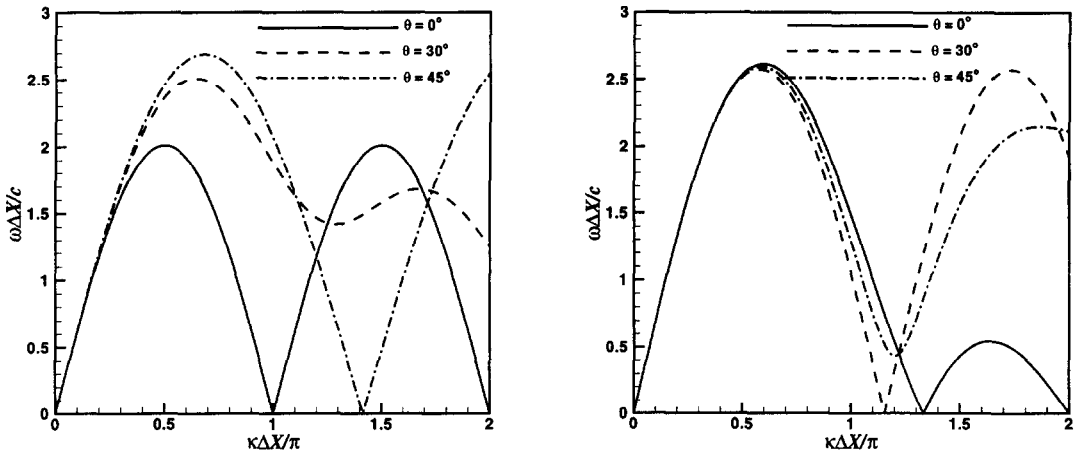

(a) Rectangular. (b) Hexagonal.

Figure 9. Frequency-wave number relations of nodal integration with Lagrangian kernel with $D_{mx} = 1.5$. $c^2 = \mu/\rho$.

Letting the current configuration be the reference configuration, so $\mathbf{F} = \mathbf{I}$, and

$$\bar{C}_{ijrl} = \lambda\delta_{ij}\delta_{rl} + \mu\left(\delta_{ir}\delta_{jl} + \delta_{il}\delta_{jr}\right) + S_{il}\delta_{jr}, \tag{4.9}$$

we can see that the tensor $\bar{\mathbf{C}}$ is not major symmetric.

Figure 9 shows the frequency as a function of relative wave number for various wave directions θ. For a rectangular arrangement of nodes with $\theta = 0$, the plot between $\kappa = 0$ and $2\pi/\Delta X$ is symmetric for $\kappa = \pi/\Delta X$ because ΔX is one side's length of quadrilateral. This is identical to what we got from 1D analysis before. From the plots, we find that no matter whether we use quadrilateral or hexagonal pattern, no tensile instability occurs. However, a spurious mode due to rank deficiency occurs for nodal integration with Lagrangian kernel.

4.1.2. Eulerian kernel

The momentum equation is

$$\begin{aligned} m_I\ddot{\tilde{u}}_i(\mathbf{x}_I) &= -\tilde{f}_{iI}^{\text{int}} \\ &= -\sum_{J\in\mathcal{N}} V_J^0\Big[\tilde{J}(\mathbf{x}_J)w_{I,j}(\mathbf{x}_J)\sigma_{ji}(\mathbf{x}_J) \\ &\quad + J(\mathbf{x}_J)\tilde{w}_{I,j}(\mathbf{x}_J)\sigma_{ji}(\mathbf{x}_J) + J(\mathbf{x}_J)w_{I,j}(\mathbf{x}_J)\tilde{\sigma}_{ji}(\mathbf{x}_J)\Big]. \end{aligned} \tag{4.10}$$

The perturbed Jacobian is

$$\tilde{J}(\mathbf{x}_J) = J(\mathbf{x}_J)\delta_{ij}\frac{\partial\tilde{u}_i(\mathbf{x}_J)}{\partial x_j} = J(\mathbf{x}_J)\delta_{st}\sum_K g_{tK}(\mathbf{x}_J)\tilde{u}_s(\mathbf{x}_K). \tag{4.11}$$

The perturbed shape function is

$$\begin{aligned} \tilde{w}_{I,j}(\mathbf{x}_J) &= w_{I,jt}(\mathbf{x}_J)\left(\tilde{u}_{Jt} - \tilde{u}_{It}\right), \\ w_{I,jt}(\mathbf{x}_J) &= \left(\frac{w_{I,rr}}{r^2} - \frac{w_{I,r}}{r^3}\right)\left(x_{Jj} - x_{Ij}\right)\left(x_{Jk} - x_{Ik}\right) + \frac{w_{I,r}}{r}\delta_{jt}, \end{aligned} \tag{4.12}$$

where

$$r = \|\mathbf{x}_J - \mathbf{x}_I\|. \tag{4.13}$$

The perturbed Cauchy stress is

$$\tilde{\sigma}_{ij} = \bar{C}'_{ijrl}\frac{\partial \tilde{u}_r}{\partial x_l} \qquad \text{or} \qquad \tilde{\sigma} = \bar{\mathbf{C}}' : \left(\mathbf{F}^{-1}\tilde{\mathbf{F}}\right). \tag{4.14}$$

In 2D plane strain,

$$C^{\sigma\mathcal{J}}_{ijrl} = \lambda\delta_{ij}\delta_{rl} + \mu\left(\delta_{ir}\delta_{jl} + \delta_{il}\delta_{jr}\right). \tag{4.15}$$

Let the current configuration be the reference configuration, $\mathbf{F} = \mathbf{I}$. So

$$\bar{C}'_{ijrl} = C^{\sigma\mathcal{J}}_{ijrl} - \sigma_{ij}\delta_{rl} + \delta_{ir}\sigma_{lj} + \sigma_{il}\delta_{jr}. \tag{4.16}$$

Substituting equations (4.11), (4.12), and (4.14) into (4.10) gives the dispersion equation

$$\begin{aligned}\omega^2 = \frac{1}{m_I(\theta_x+\theta_y)}\sum_{i\in 2}\sum_{J\in\mathcal{N}} V_J^0 \left[w_{I,j}(\mathbf{x}_J)\bar{C}'_{ijrl}\theta_r S_l(\mathbf{x}_J)\right. \\ \left. + w_{I,j}(\mathbf{x}_J)\sigma_{ij}(\mathbf{x}_J)\theta_t S_t(\mathbf{x}_J) + \sigma_{ij}(\mathbf{x}_J)w_{I,jt}(\mathbf{x}_J)\theta_t(c_{JI}-1)\right],\end{aligned} \tag{4.17}$$

where

$$\begin{aligned}S_i(\mathbf{x}_J) &= \sum_K g_{iK}(\mathbf{x}_J)c_{KI}, \\ c_{JI} &= \cos[\kappa(x_J\theta_x + y_J\theta_y) - \kappa(x_I\theta_x + y_I\theta_y)].\end{aligned} \tag{4.18}$$

Figure 10 shows the relationships between frequency and wave number for nodal integration with an Eulerian kernel. When the tensile stress is normalized by $\bar{\sigma} = \sigma/\mu = 1.0$, we can see that the discretization is unstable for $\theta = 30°$ and $45°$. It is tensile instability for nodal integration with Eulerian kernel. That is what we get from 1D analysis.

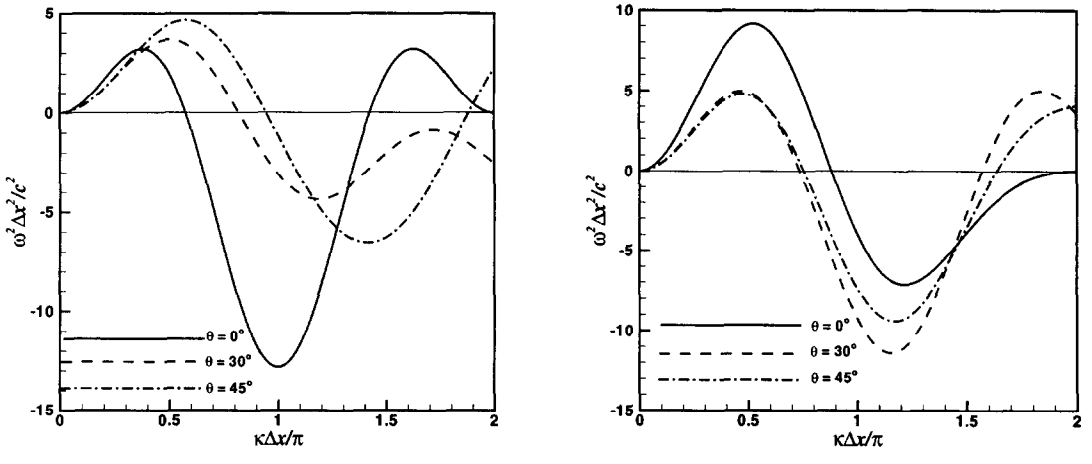

(a) Rectangular. (b) Hexagonal.

Figure 10. Frequency-wave number relations for nodal integration with Eulerian kernel for $D_{mx} = 1.5$, $c^2 = \mu/\rho$.

4.2. Stress Points

4.2.1. Lagrangian kernel

In 2D, for stress points integration with Lagrangian kernel, the perturbed momentum equation is

$$\begin{aligned}m_I\ddot{\tilde{u}}_i\left(\mathbf{X}_I^m\right) &= -\tilde{f}_{iI}^{\text{int}} \\ &= -\sum_{J\in\mathcal{N}_M} V_J^{0m} w_{I,j}\left(\mathbf{X}_J^m\right)\tilde{P}_{ji}\left(\mathbf{X}_J^m\right) - \sum_{J\in\mathcal{N}_S} V_J^{0s} w_{I,j}\left(\mathbf{X}_J^s\right)\tilde{P}_{ji}\left(\mathbf{X}_J^s\right).\end{aligned} \tag{4.19}$$

Substituting equation (4.2) into equation (4.19), the stability equation for stress points with Lagrangian kernel is

$$\omega^2 = \frac{1}{m_I(\theta_X+\theta_Y)} \sum_{i\in 2} \sum_{J\in\mathcal{N}_M} V_J^{0m} w_{I,j}\left(\mathbf{X}_J^m\right) \bar{C}_{ijrl}\theta_r S_l\left(\mathbf{X}_J^m\right) + \frac{1}{m_I(\theta_X+\theta_Y)} \sum_{i\in 2} \sum_{J\in\mathcal{N}_S} V_J^{0s} w_{I,j}\left(\mathbf{X}_J^s\right) \bar{C}_{ijrl}\theta_r S_l\left(\mathbf{X}_J^s\right), \tag{4.20}$$

where

$$S_i\left(\mathbf{X}_J^m\right) = \sum_K G_{lK}\left(\mathbf{X}_J^m\right) c_{KI}, \qquad S_i\left(\mathbf{X}_J^s\right) = \sum_K G_{lK}\left(\mathbf{X}_J^s\right) c_{KI}. \tag{4.21}$$

Figure 11 shows the plots for the frequency as a function of normalized wave number for various propagation directions. No tensile instability occurs for stress point integration with Lagrangian kernel.

For rectangular pattern (Figure 11a), the discretization is unstable for $\theta = 45°$ at the cut off wave number. This is a spurious singular mode rather than a tensile instability: it occurs even if the stress vanishes.

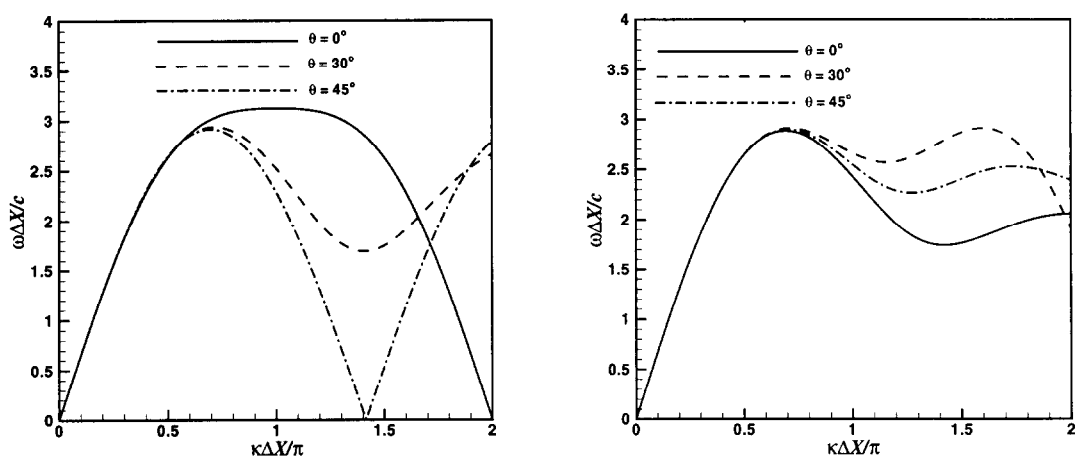

(a) Rectangular. (b) Hexagonal.

Figure 11. Frequency-wave number relations of stress point with Lagrangian kernel for $D_{mx} = 1.5$, $c^2 = \mu/\rho$.

4.2.2. Eulerian kernel

In 2D, for stress points integration with Eulerian kernel, the perturbed momentum equation is

$$\begin{aligned} m_I \ddot{\tilde{u}}_i\left(\mathbf{X}_I^m\right) = &- \sum_{J\in\mathcal{N}_M} V_J^{0m} \left[\tilde{J}\left(\mathbf{x}_J^m\right) w_{I,j}\left(\mathbf{x}_J^m\right) \sigma_{ij}\left(\mathbf{x}_J^m\right) + J\left(\mathbf{x}_J^m\right) \tilde{w}_{I,j}\left(\mathbf{x}_J^m\right) \sigma_{ij}\left(\mathbf{x}_J^m\right) \right. \\ &\left. + J\left(\mathbf{x}_J^m\right) w_{I,j}\left(\mathbf{x}_J^m\right) \tilde{\sigma}_{ij}\left(\mathbf{x}_J^m\right)\right] \\ &- \sum_{J\in\mathcal{N}_S} V_J^{0s} \left[\tilde{J}\left(\mathbf{x}_J^s\right) w_{I,j}\left(\mathbf{x}_J^s\right) \sigma_{ij}\left(\mathbf{x}_J^s\right) + J\left(\mathbf{x}_J^s\right) \tilde{w}_{I,j}\left(\mathbf{x}_J^s\right) \sigma_{ij}\left(\mathbf{x}_J^s\right) \right. \\ &\left. + J\left(\mathbf{x}_J^s\right) w_{I,j}\left(\mathbf{x}_J^s\right) \tilde{\sigma}_{ij}\left(\mathbf{x}_J^s\right)\right]. \end{aligned} \tag{4.22}$$

From equations (4.11), (4.12), and (4.14), for $\mathbf{x}_J = \mathbf{x}_J^m$ or $\mathbf{x}_j^s$, we have

$$\begin{aligned}
\tilde{J}(\mathbf{x}_J) &= J(\mathbf{x}_J)\,\delta_{ij}\frac{\partial \tilde{u}_i(\mathbf{x}_J)}{\partial x_j} = J(\mathbf{x}_J)\,\delta_{st}\sum_K g_{tK}(\mathbf{x}_J)\,\tilde{u}_s(\mathbf{x}_K),\\
\tilde{w}_{I,j}(\mathbf{x}_J) &= w_{I,jt}(\mathbf{x}_J)\left(\tilde{u}_t(\mathbf{x}_J) - \tilde{u}_t(\mathbf{x}_I^m)\right),\\
\tilde{\sigma}_{ij}(\mathbf{x}_J) &= \bar{C}'_{ijrl}\frac{\partial \tilde{u}_r(\mathbf{x}_J)}{\partial x_l} = \bar{C}'_{ijrl}\sum_K g_{lK}(\mathbf{x}_J)\tilde{u}_r(\mathbf{x}_K^m)
\end{aligned} \tag{4.23}$$

because

$$u(\mathbf{x}_J^s) = \sum_K w_K(\mathbf{x}_J^s)\,u(\mathbf{x}_K^m). \tag{4.24}$$

Letting the current configuration be the reference configuration, $u(\mathbf{x}_K^m) = 0$, then we can get the perturbed displacement for slave nodes by the following approximation:

$$\tilde{u}(\mathbf{x}_J^s) = \sum_K w_K(\mathbf{x}_J^s)\,\tilde{u}(\mathbf{x}_K^m). \tag{4.25}$$

Substituting equation (4.25),(4.23) into equation (4.22), we get the dispersion equation for stress points with Eulerian kernel

$$\begin{aligned}
\omega^2 = {} & \frac{1}{m_I(\theta_x+\theta_y)}\sum_{i\in 2}\sum_{J\in\mathcal{N}_m} V_J^{0m}\left[w_{I,j}(\mathbf{x}_J^m)\,\bar{C}'_{ijrl}\theta_r S_l(\mathbf{x}_J^m)\right.\\
& \left. + w_{I,j}\sigma_{ij}(\mathbf{x}_J^m)\,\theta_t S_t(\mathbf{x}_J^m) + \sigma_{ij}(\mathbf{x}_J^m)\,w_{I,jt}(\mathbf{x}_J^m)\,\theta_t(c_{JI}-1)\right]\\
& + \frac{1}{m_I(\theta_x+\theta_y)}\sum_{i\in 2}\sum_{J\in\mathcal{N}_s} V_J^{0s}\left[w_{I,j}(\mathbf{x}_J^s)\,\bar{C}'_{ijrl}\theta_r S_l(\mathbf{x}_J^s) + w_{I,j}(\mathbf{x}_J^s)\,\sigma_{ij}(\mathbf{x}_J^s)\,\theta_t S_t(\mathbf{x}_J^s)\right.\\
& \left. + \sigma_{ij}(\mathbf{x}_J^s)\,w_{I,jt}(\mathbf{x}_J^s)\,\theta_t\left(\sum_K w_K(\mathbf{x}_J^s)\,c_{KI} - 1\right)\right],
\end{aligned} \tag{4.26}$$

where

$$S_i(\mathbf{x}_J) = \left(\sum_K g_{iK}(x_J)\,c_{KI}\right). \tag{4.27}$$

Figure 12 shows relationships between the frequency and wave number for stress points with Eulerian kernel. The tensile stress is $\bar{\sigma} = \sigma/\mu = 2.0$. We find that the tensile instability is not eliminated by stress points for an Eulerian kernel in 2D. In 1D, we found stress points eliminate the tensile instability.

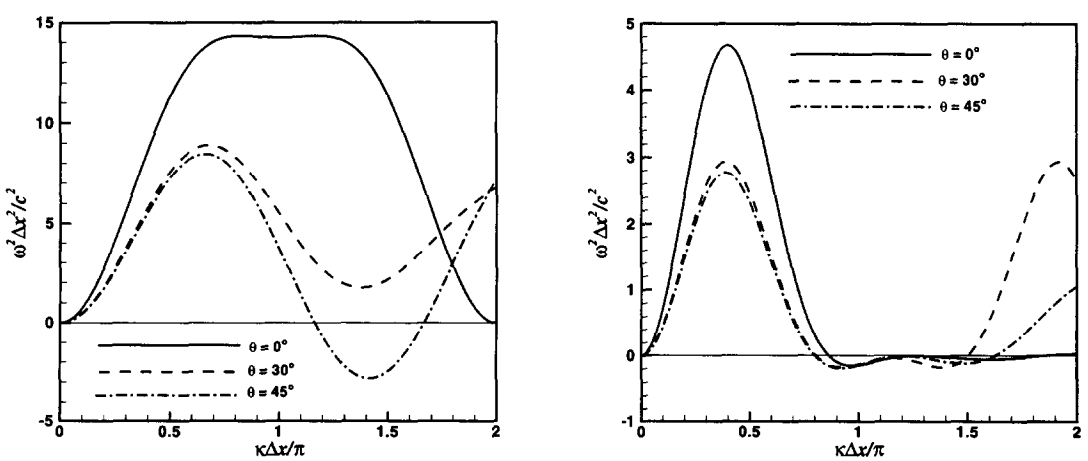

(a) Rectangular. (b) Hexagonal.

Figure 12. Frequency-wave number relations of stress points with Eulerian kernel for $D_{mx} = 1.5$. $c^2 = \mu/\rho$.

5. NUMERICAL EXAMPLES

5.1. One-Dimensional Stability

We consider a simple 1D example to verify our analysis of the tensile instability. A rod is fixed at both ends, and an initial stress is prescribed, $\sigma_0 = 1.0\,\text{GPa}$. The center node of the rod is given an initial velocity, $v_0 = 40\,\text{m/s}$. Nodal integration is used with Eulerian and Lagrangian kernels. The material constants are density $\rho = 2450\,\text{kg/m}^3$, Young's modulus $E = 10.0\,\text{GPa}$, the length of the rod $l = 0.04\,\text{m}$.

The velocity at the center node of rod is shown in Figure 13. From Figure 13, we see that the tensile instability occurs for the Eulerian kernel but not the Lagrangian kernel (note the velocity for the Eulerian kernel is ten times larger).

For the Eulerian kernel with $D_{mx} = 2.5$, there is no tensile instability when the initial stress is the same ($\bar{\sigma} = 0.1$) as above. However, upon increasing the initial stress so that $\bar{\sigma} = 0.16$, the tensile instability is found again.

We also examine this problem with slave nodes (stress points) between the original nodes using Lagrangian kernel and Eulerian kernel with $D_{mx} = 1.5$. The problem was studied for $\bar{\sigma} \in [0.0, 1.0]$. In all cases, the tensile instability is eliminated by stress points integration.

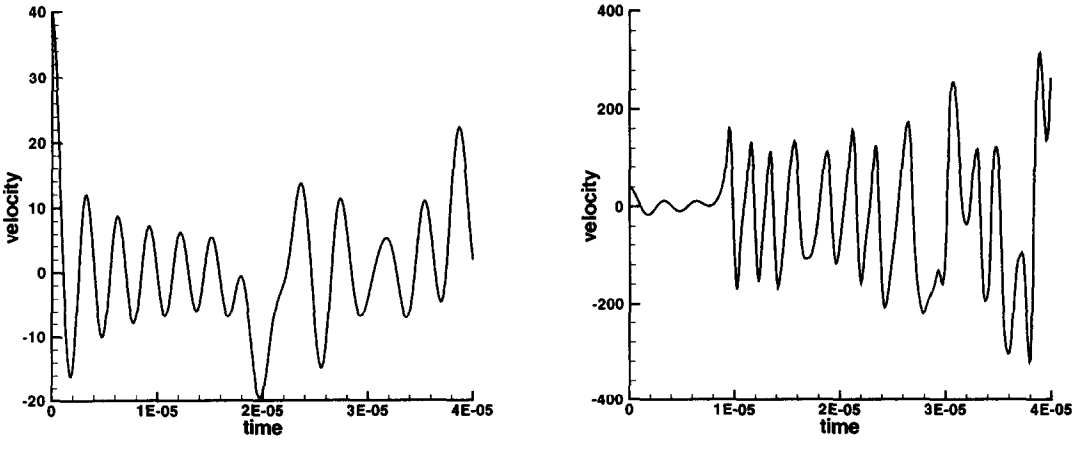

(a) Lagrangian kernel.

(b) Eulerian kernel.

Figure 13. Velocity at center of prestressed rod with nodal integration for $D_{mx} = 1.5$ showing the instability in the Eulerian kernel.

5.2. Two-Dimensional Demonstration

This example shows the onset of a tensile instability for an Eulerian kernel in a 2D problem. We use a hyperelastic material [23]

$$\boldsymbol{\sigma} = \frac{1}{\sqrt{I_3}} \left[(c_1 + c_2 I_1)\mathbf{B} - c_2 \mathbf{B}^2 - \left(c_1 I_3^{1/3} + 2c_2 I_3^{2/3} - \lambda \ln I_3 \right) \mathbf{I} \right], \tag{5.1}$$

where $\mathbf{B} = \mathbf{F}\mathbf{F}^{\mathsf{T}}$. The material constants are $c_1 = 1.265e5\,\text{N/m}^2$, $c_2 = 1.012e4\,\text{N/m}^2$, and $\lambda = 1.012e7\,\text{N/m}^2$. $I_1 = \text{tr}(\mathbf{B})$ and $I_3 = \det(\mathbf{B})$. The material density is $\rho = 125.4\,\text{Kg/m}^3$.

A pressure of $6.2e7\,\text{N/m}^2$ is applied for 0.1 ms on the inner surface of the rubber ring; 1040 particles are used for nodal integration. The discrete model with stress points consists of 540 master nodes and 480 slave nodes. Figure 14 shows the deformed rubber ring at the same time by Lagrangian kernel and Eulerian kernel with nodal integration. Figure 15 shows the results with the stress point formulation. Figures 14b and 15b show the clustering of particles in the Eulerian kernel which is typical of the tensile instability.

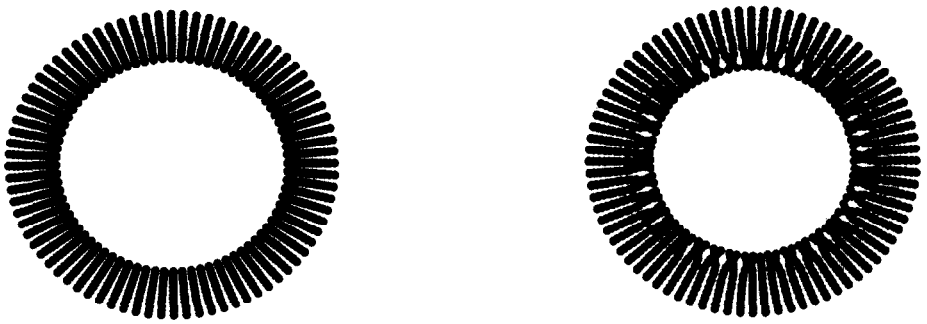

(a) Lagrangian kernel. (b) Eulerian kernel.

Figure 14. Deformed rubber ring by nodal integration ($t = 0.16$ ms).

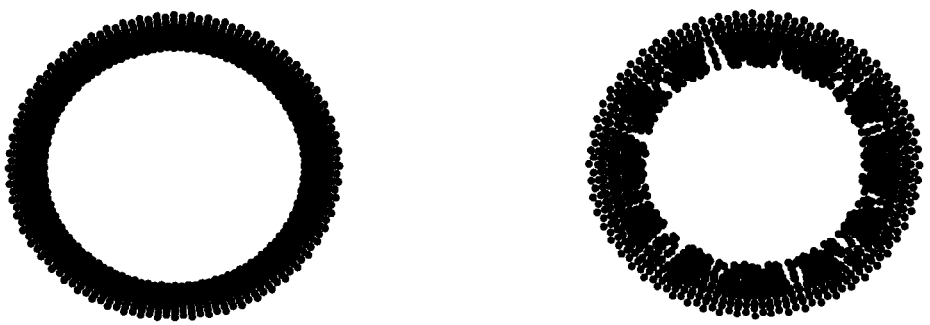

(a) Lagrangian kernel. (b) Eulerian kernel.

Figure 15. Deformed rubber ring by stress points ($t = 0.12$ ms).

5.3. Material Instability

Here we will show the performance of Lagrangian and Eulerian kernels for a shear band problem. A J_2 flow constitutive model is used, and the stress rate relation is

$$\boldsymbol{\tau}^{\nabla J} = C_{el}^{\tau J} : \mathbf{D}^e = C_{el}^{\tau J} : (\mathbf{D} - \mathbf{D}^p)\,. \tag{5.2}$$

The yield condition is

$$f(\boldsymbol{\tau}, \mathbf{q}) = \bar{\sigma} - \sigma_Y(\bar{\varepsilon}) = 0,$$
$$\frac{\partial f}{\partial \boldsymbol{\tau}} = \frac{3}{2\bar{\sigma}}\boldsymbol{\tau}^{\mathrm{dev}}, \qquad \frac{\partial f}{\partial \bar{\varepsilon}} = -\frac{d}{d\bar{\varepsilon}}\sigma_Y(\bar{\varepsilon}) = -H(\bar{\varepsilon}),$$

where $\sigma_Y(\bar{\varepsilon})$ is the yield stress in uniaxial tension, $\bar{\varepsilon}$ is the effective plastic strain, $\bar{\sigma}$ is the von Mises effective stress which is $[(3/2)\boldsymbol{\tau}^{\mathrm{dev}} : \boldsymbol{\tau}^{\mathrm{dev}}]^{1/2}$, and $H(\bar{\varepsilon})$ is the plastic modulus. For softening material which is unstable material, H is negative.

The steel ring loaded by an increasing pressure ($2.0e8\,\mathrm{N/m^2}$ per ms) is used. The material constants are $\rho = 7800\,\mathrm{Kg/m^3}$, $E = 2.0e11\,\mathrm{N/m^2}$, $H = -E/10$, $\sigma_Y(0) = 2.0e8\,\mathrm{N/m^2}$. 1050 nodes are used in nodal integration, and an additional 900 slave nodes are used for stress point.

Figures 16 and 17 show the distribution of the effective strain in the deformed steel ring. We found that the shear bands occur because of the instability material [15]. From [24], we know the field of shears bands around a circular hole loaded uniform pressure because at every point of the field, the principal stress coincides to radial and circumference directions. The shear bands will be logarithmic spirals emerging from the inner surface at an angle $\pm\pi/4$.

Regardless of whether we use nodal integration or stress points, the shear bands we obtained have the property we mentioned above for both Lagrangian kernel and Eulerian kernel. When a

(a) Lagrangian kernel. (b) Eulerian kernel.

Figure 16. Deformed steel ring by nodal integration ($t = 0.4$ ms).

(a) Lagrangian kernel. (b) Eulerian kernel.

Figure 17. Deformed steel ring by stress points ($t = 0.4$ ms).

shear band has grown across the ring, the system will be unstable; i.e, the ring will break into fragments [25–27].

The shear bands usually are initiated where stress or strain concentrations occur due to geometry or material inhomogeneity. In a numerical simulation with uniformly distributed stress, a slight imperfection from either material or numerical may trigger the localization. So shear bands will occur at different positions and on different patterns for different methods. With Eulerian kernel, the positions of shear bands differ from with Lagrangian kernel because of these effects.

In this problem, slight differences are introduced by the Eulerian kernel, but the differences are not severe. The material instability occurs suddenly due to the rapid decrease in the material modulus in the material model.

6. CONCLUSION

A stability analysis of the particle method with corrected derivatives has been presented. The stability properties of the particle method with Eulerian and Lagrangian kernels under nodal integration and stress points integration were investigated using Fourier analysis in one dimension. In two dimensions, the stability of stress points integration with Lagrangian kernel was also studied.

We have shown that in a plane wave one-dimensional analysis, two types of instability occur in the particle methods:

(1) an instability which occurs due to rank deficiency of the discretization of the divergence and makes the equilibrium equations singular; this occurs regardless of the value of the stress;
(2) a material instability, which should be present since it occurs in the governing PDEs.

However, Eulerian kernels severely distort the material instability; this is manifested in one dimension in the tensile instability.

Several findings are noteworthy.

(1) The tensile instability only occurs with an Eulerian kernel; for a Lagrangian kernel, only the material instabilities occur.

(2) In one dimension, stress points eliminate the instability due to rank deficiency. However, in two dimensions, the stabilization depends on the arrangement and number of stress points. For the straightforward scheme where stress points are placed at the center of virtual quadrilateral generated by the initial positions of the particles, the rank deficiency instability persists. For adequate stabilization of this spurious mode, stress points must be placed in virtual triangles generated by particle positions; i.e., the density of the stress points must be greater than that resulting from virtual quadrilaterals. The implications of this finding to three-dimensional stress point stabilization require further study.

From this study, we conjecture that the best approach to stable particle discretizations of solids and fluids is to use Lagrangian kernels with stress points. Lagrangian kernel functions may be limited in the distortions they can tolerate. However, if the distortions are severe, reinitialization of the Lagrangian kernel can always be done.

REFERENCES

1. T. Belytschko, Y.-Y. Lu and L. Gu, Element-free Galerkin methods, *Int. J. Numer. Meth. Engng.* **37**, 229–256, (1994).
2. C.A. Duarte and J.T. Oden, HP clouds—A meshless method to solve boundary-value problems, Technical Report 95-05, University of Texas at Austin, (1995).
3. C.A. Duarte and J.T. Oden, An H-P adaptive method using clouds, *Comput. Meths. Appl. Mech. Engrg.* **139**, 237–262, (1996).
4. L.B. Lucy, A numerical approach to the testing of the fission hypothesis, *J. Astron.* **82**, 1013–1024, (1977).
5. J.J. Monaghan, An introduction to SPH, *Comput. Phys. Commun.* **48**, 89–96, (1988).
6. T. Belytschko, K. Krongauz, D. Organ, M. Fleming and P. Krysl, Meshless methods: An overview and recent developments, *Comput. Meths. Appl. Mech. Engrg.* **139**, 3–47, (1996).
7. W.K. Liu, S.F. Li and T. Belytschko, Moving least square reproducing kernel method. (I) Methodology and convergence, *Comput. Meths. Appl. Mech. Engrg.* **143**, 113–154, (1997).
8. G.R. Johnson and S.R. Beissel, Normalized smoothing functions for SPH impact calculations, *Int. J. Numer. Meth. Engng.* **39**, 2725–2741, (1996).
9. P. Randles and L. Libersky, Smoothed particle hydrodynamics: Some recent improvements and applications, *Comput. Meths. Appl. Mech. Engrg.* **139**, 375–408, (1996).
10. Y. Krongauz and T. Belytschko, Consistent pseudo-derivatives in meshless methods, *Comput. Meth. Appl. Mech. Engng.* **146**, 371–386, (1968).
11. T. Belytschko, K. Krongauz, J. Dolbow and C. Gerlach, On the completeness of meshfree particle methods, *Int. J. Numer. Meth. Engng.* **43**, (1998).
12. T. Black and T. Belytschko, Convergence of corrected derivative methods for second-order linear partial differential equations, *Int. J. Numer. Meth. Engng.* **44**, 177–203, (1999).
13. C.T. Dyka and R.P. Ingel, An approach for tension instability in smoothed particle hydrodynamics (SPH), *Comput. Struct.* **57**, 573–580, (1995).
14. C.T. Dyka, P.W. Randles and R.P. Ingel, Stress points for tension instability in SPH, *Int. J. Numer. Meth. Engng.* **40**, 2325–2341, (1997).
15. T. Belytschko, W.K. Liu and B. Moran, *Finite Element Methods for Nonlinear Continua and Structures*, Wiley, New York, (2000).
16. D. Shepard, A two dimensional function for irregularly spaced data, *ACM National Conf.*, (1968).
17. T. Belytschko, Y. Krongauz, J. Dolbow and C. Gerlach, On the completeness of meshfree particle methods, *Int. J. Numer. Mech. Engng.* **43**, 785–819, (1998).
18. S. Beissel and T. Belytschko, Nodal integration of the element-free Galerkin method, *Comput. Meths. Appl. Mech. Engrg.* **139**, 49–74, (1996).
19. R. Seydel, *From Equilibrium to Chaos, Practical Bifurcation and Stability Analysis*, Elsevier, New York, (1988).
20. J.M.T. Thompson and G.W. Hunt, *Elastic Instability Phenomena*, Chichester, Wiley, New York, (1984).
21. R.W. Ogden, *Non-Linear Elastic Deformations*, Ellis Horwood, (1984).
22. J.W. Swegle, D.L. Hicks and S.W. Attaway, Smoothed particle hydrodynamics stability analysis, *J. Comput. Phys.* **116**, 123–134, (1995).

23. L.M. Kachanov, Time of the rupture process under creep conditions, *Izv. Akad. Nauk SSR Otd. Tech.* **Nauk 8**, 26–31, (1958).
24. L.M. Kachanov, *Foundations of the Theory of Plasticity*, North Holland, London, (1971).
25. D.E. Grady and D.A. Benson, Fragmentation of metal rings by electromagnetic loading, *Exp. Mech.* **12**, 393–400, (1983).
26. N.F. Mott, Fragmentation of shell cases, *Proc. Roy. Soc. London* **300**, 300–308, (1947).
27. S. Hao, W.K. Liu and C.T. Chang, Computer implementation of damage models by finite element and meshfree methods, *Comput. Meths. Appl. Mech. Engrg.* **187**, 401–440, (2000).
28. I. Fried and A.R. Johnson, A note on elastic energy density function for largely deformed compressible rubber solids, *Comput. Meths. Appl. Mech. Engrg.* **69**, 53–64, (1988).